Resonant amplification of subinertial tides in a submarine canyon

N. C. Swart,[1,2] S. E. Allen,[1] and B. J. W. Greenan[3]

Received 31 January 2011; revised 7 May 2011; accepted 7 June 2011; published 2 September 2011.

[1] Tidal oscillations dominate the flow field in many submarine canyons. Observations have shown that semidiurnal tidal energy in submarine canyons is significantly amplified with respect to adjacent shelves. This amplification is thought to be caused by focusing of propagating internal tides incident from the open ocean, or local in-canyon generation on critical canyon floor slopes. These mechanisms require freely propagating internal tides, with superinertial frequencies. We present results from a moored array in a canyon at 44°N, where the observed velocities reached over 0.8 m s^{-1}. The canyon flow field was highly unusual because it was dominated by the subinertial diurnal tide. This occurred despite the fact that the barotropic tide was predominantly semidiurnal. The diurnal tide was dramatically amplified in the canyon, its velocities increasing toward the seafloor and canyon head. The diurnal oscillations also exhibited marked modulation in time by the background barotropic forcing. Length scales suggest that the diurnal tide should be resonant in the canyon. An analytical framework is used to explain the mechanisms behind the strong diurnal currents observed by the moored array. In the model, along-shelf barotropic flow sets up a double Kelvin wave response in the canyon, generating along-canyon velocities which are subsequently amplified by resonance. The pattern of the model predictions is in excellent agreement with the observed velocity pattern.

Citation: Swart, N. C., S. E. Allen, and B. J. W. Greenan (2011), Resonant amplification of subinertial tides in a submarine canyon, *J. Geophys. Res.*, *116*, C09001, doi:10.1029/2011JC006990.

1. Introduction

1.1. Canyons and the General Circulation

[2] Submarine canyons are ubiquitous features on the continental shelf. They occupy on average about 20% of the North and Central American coastline, but in places up to half of the shelf edge is incised with these features [*Hickey*, 1995]. Moored current meters have shown that the flow field within canyons is typically dominated by along-axis flow at near tidal frequencies [*Shepard et al.*, 1979]. Diverse observations have also demonstrated that tidal energy is amplified in canyons relative to the surrounding shelf [*Shepard et al.*, 1979; *Hotchkiss and Wunsch*, 1982; *Petruncio et al.*, 1998; *Kunze et al.*, 2002; *Lee et al.*, 2009]. Intense tidal motions within canyons result in enhanced bottom mixing [*Carter and Gregg*, 2002; *Lee et al.*, 2009], which in turn has significant implications for shelf-ocean exchange [*McPhee-Shaw*, 2006; *Allen and Durrieu de Madron*, 2009] and local ecosystems [*Thomsen and van Weering*, 1998; *Monteiro et al.*, 2005]. The dissipation is also a sink in the global tidal energy budget [*Munk*, 1997], and the resulting mixing is a driver of the meridional overturning circulation [*Wunsch and Ferrari*, 2004].

[3] In stratified shelf systems, tidal flow over abrupt shelf break topography frequently generates internal waves at the tidal period [*Wunsch*, 1975]. These baroclinic motions contribute to the observed tidal amplification in canyons [*Petruncio et al.*, 2002]. Internal tides are affected by rotation, and the wave energy travels in beams or characteristics at an angle ϕ_g to the horizontal, perpendicular to the wave crests. This angle is determined by the frequency of the internal waves, the vertical density structure and the latitude

$$\tan(\phi_g) = \left[\frac{\omega^2 - f^2}{N^2 - \omega^2}\right]^{1/2} \quad (1)$$

where ω is the internal wave frequency; f is the Coriolis frequency, and N is the buoyancy frequency [*Gill*, 1982].

[4] A limit on the lower end of the permitted frequency range of free waves is given by inertial oscillations at $T = 2\pi/|f|$. Thus in general $\omega > |f|$ for free internal waves. A wave propagating poleward cannot pass the latitude where $\omega = |f|$, and will be reflected there. Forced motions such as tides might produce internal waves with $\omega < |f|$ to satisfy boundary conditions, however these waves will be bottom trapped and will decay exponentially away from the seafloor. Further, these trapped waves will not propagate, although they will be periodic in time [*Gill*, 1982; *Pond and Pickard*, 1983].

[1]Department of Earth and Ocean Science, University of British Columbia, Vancouver, British Columbia, Canada.
[2]Now at School of Earth and Ocean Sciences, University of Victoria, Victoria, British Columbia, Canada.
[3]Ocean Circulation Section, Ocean Sciences Division, Fisheries and Oceans Canada, Bedford Institute of Oceanography, Dartmouth, Nova Scotia, Canada.

0148-0227/11/2011JC006990

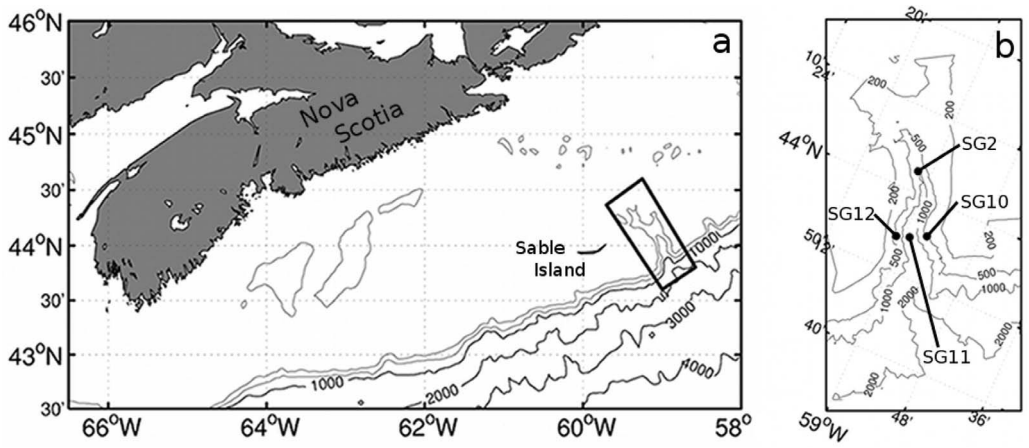

Figure 1. (a) The bathymetry of the Scotian Shelf of eastern Canada. The inset box to the east of Sable Island denotes the position of the Gully. (b) A high-resolution bathymetry of the boxed region inset in Figure 1a showing the sinuous Sable Gully. Black dots denote mooring positions. Contours are at 200, 500, 1000, and 2000 m.

[5] When interacting with a flat bottom, the surface, or the base of the pycnocline, freely propagating internal waves are reflected with an angle equal to the angle of incidence, relative to the local gravity vector [*Cacchione et al.*, 2002]. In the case of a bottom sloping at an angle γ, the waves may either be reflected ($\gamma/\phi_g > 1$) or transmitted ($\gamma/\phi_g < 1$). In the special case where $\gamma/\phi_g = 1$, the so called critical angle, the energy of the internal wave is trapped near the bottom, leading to maximum bottom velocities and shear stresses [*Cacchione and Drake*, 1986; *Cacchione et al.*, 2002; *McPhee-Shaw et al.*, 2004; *Wunsch*, 1969].

[6] Submarine canyons often exhibit a v-shaped topography [*Shepard et al.*, 1979]. That is, the width of the canyon decreases with depth. The canyon width also typically decreases toward the head. The reduction in volume causes a geometric funneling and linear amplification of energy traveling toward the canyon head. This funneling effect offers a partial explanation for tidal amplification within canyons. Geometric focusing of internal tidal energy is a separate, complementary mechanism for the observed amplification. Freely propagating internal wave energy is focused to the bottom of canyons by successive supercritical reflections from the steep canyon side walls [*Gordon and Marshall*, 1976]. Similarly, internal wave energy encroaching on the shelf from the open ocean will be focused by successive reflections toward the canyon head [*Hotchkiss and Wunsch*, 1982]. Note that this mechanism requires freely propagating internal waves, which poleward of 30°, precludes the diurnal internal tide by (1).

[7] The available observations [*Hotchkiss and Wunsch*, 1982; *Huthnance*, 1989; *Petruncio et al.*, 1998; *Kunze et al.*, 2002; *Wang et al.*, 2008; *Lee et al.*, 2009] show an increase in tidal energy toward the bottom, and head of the respective canyons. The observed amplification usually exceeded that expected from linear geometrical funneling, invoking the internal tide focusing mechanism. The observations also unanimously demonstrate a dominance of the M_2 tide within canyons. This presumably relates to their latitude (>30°), and the exclusion of free waves at the diurnal frequency. Laboratory [*Baines*, 1983] and numerical [*Petruncio et al.*, 2002] experiments have attempted to explore the parameter space of variables controlling the degree of tidal amplification. The broad conclusion that can be drawn is that the degree of amplification is sensitive to the canyon bottom slope. Greater areas of critical bottom slope result in more intense tides [*Petruncio et al.*, 2002]. However, the early laboratory study neglected rotation and had simple geometry [*Baines*, 1983]. The numerical experiment [*Petruncio et al.*, 2002] was also limited to simple geometries, and had only partial success in reproducing the observations [*Kunze et al.*, 2002]. *Pérenne et al.* [2001] and *Boyer et al.* [2004] investigated oscillatory flows over submarine canyons using laboratory and numerical models, with a simple geometry and realistic stratification. The focus in those studies was on the mean flow in a canyon that was both shorter and shallower than the canyon we are interested in here and the nature of the time-evolving tidal flow for long canyons remains unclear from the *Boyer et al.* [2004] results. The understanding of tidal amplification in submarine canyons is as yet incomplete.

[8] In this paper we describe mooring observations of canyon tidal amplification that demonstrate a highly unusual dominance of the K_1 frequency, despite the high latitude (44°N). As far as we are aware, this is a previously unobserved phenomena. In order to understand the dynamical mechanisms behind the observed amplification, we develop and apply an analytical modeling framework.

1.2. The Gully Region

[9] The Gully is located on the Scotian Shelf of Canada, east of Sable Island. It is a broad deep canyon, reaching 2000 m deep and 15 km wide near its mouth, and narrowing significantly along its sinuous axis toward the head (see Figure 1). The Gully's steep walls are reflective for tidal frequencies, and the floor maybe transmissive, critical or reflective depending on the stratification. Numerical results suggest that water rotates in a cyclonic gyre within the Gully [*Han and Loder*, 2003], which is occasionally perturbed by the influence of Gulf Stream Rings [*Strain and Yeats*, 2005]. The surface tide is dominated by the M_2 and K_1 components, with a typical range of over 1 m.

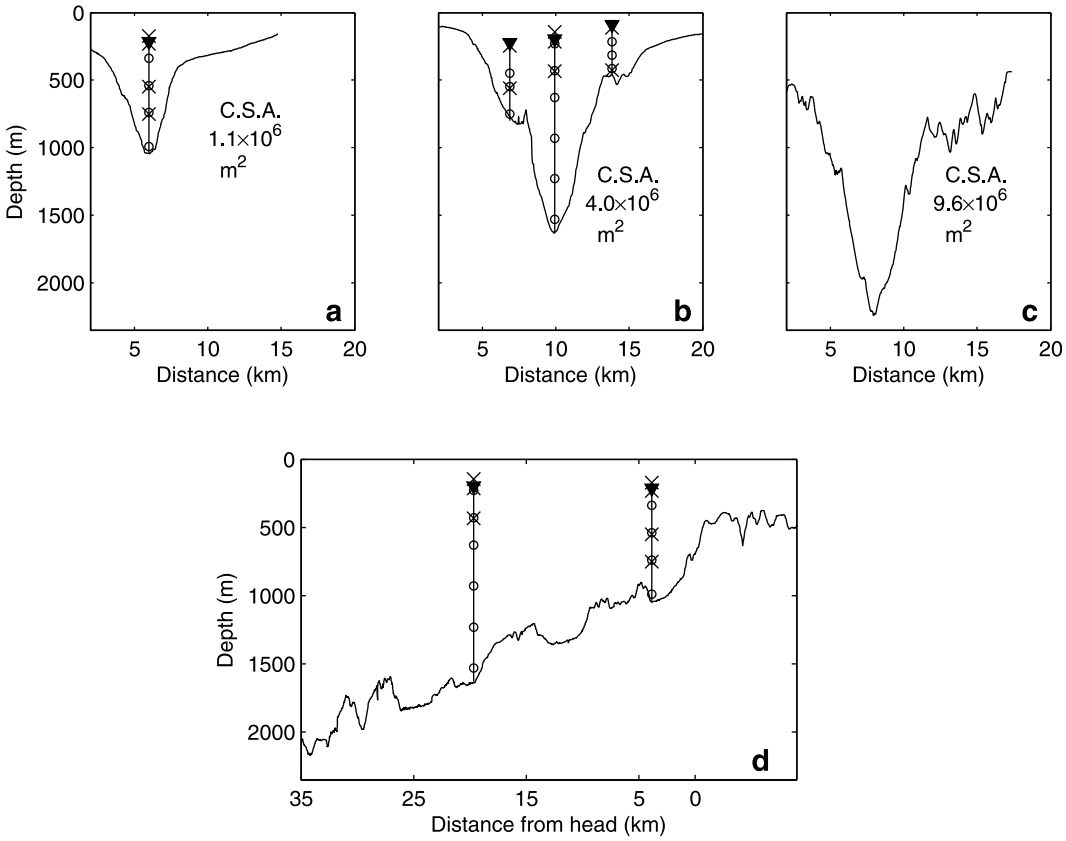

Figure 2. Bathymetric cross sections of the Gully at (a) 5 km from the head, inline with the mooring SG2; (b) 20 km from the head, inline with the moorings near the canyon center; and (c) at the canyon mouth, defined by the 500 m isobath. An estimate of the cross-sectional area below the 500 m isobath is given for each section. (d) A bathymetric profile along the axis of the Gully. The positions of the moorings are shown, and instruments utilized are represented as follows: RCMs (circles), CTDs (crosses), and ADCPs (inverted triangles).

[10] Elevated levels of nutrients [*Strain and Yeats*, 2005] and organic carbon have been observed near the head of the Gully, perhaps explaining the unusually high density of demersal fish, cetaceans and seals found in the Gully region [*Gordon and Fenton*, 2002]. High concentrations of organic carbon at the head, and along the axis of the Gully, also suggest that the canyon may act as a conduit for the production and export of organic matter to the deep ocean [*Gordon and Fenton*, 2002]. The benthos also exhibit high diversity in the Gully, purportedly due to the range of available habitats on the canyon walls [*Strain and Yeats*, 2005]. The richness of the ecosystem lead to the Gully being declared a Marine Protected Area (MPA) in 2004. The physical mechanism responsible for the vertical nutrient transport required to sustain the enhanced productivity in the Gully remains in question. Canyon upwelling is not a candidate, because the large scale mean circulation makes the Gully a downwelling canyon.

[11] Internal tides have, however, been known to influence the nutrient dynamics of the Scotian Shelf [*Sandstrom and Elliot*, 1984]. *Sandstrom and Elliot* [2002] showed that semidiurnal tidal energy was elevated at least threefold in the Gully compared to the surrounding shelf. Within the Gully itself, tidal amplification was concentrated on the eastern edge, where higher rates of turbulent mixing were observed. These rates of energy dissipation were calculated to be greater than that of a 30 m s^{-1} wind, and thus internal tide dissipation is the dominant mixing process during favorable stratification in spring and summer. The high rates of mixing induced by baroclinic tidal dissipation on the eastern edge of the Gully correlates with elevated nutrient concentrations [*Strain and Yeats*, 2005]. Here we present current meter observations from a moored array that contributes to a modified picture of tidal activity and vertical mixing in the Gully.

2. Data and Methods

[12] An array of four moorings was maintained in the Gully between April 2006 and August 2007. Each mooring was instrumented with Aanderaa RCM8 current meters, Sea-Bird SBE 37 MicroCAT CTDs, and upward looking 300 kHz RDI ADCPs near the surface (B. Greenan et al., Physical, chemical and biological variability of the Sable Gully 2006–07, report in preparation, 2011). Figure 1 shows the locations of the moorings, and Figure 2 includes schema of the instrument positions. In the present paper we use the CTD, RCM, and ADCP data, at hourly intervals, over the period 18 June 2006 at 05:00 to 15 June 2007 at 16:00.

[13] During the deployment the moorings on the axis of the canyon (SG2, near the canyon head; and S11, on the axis

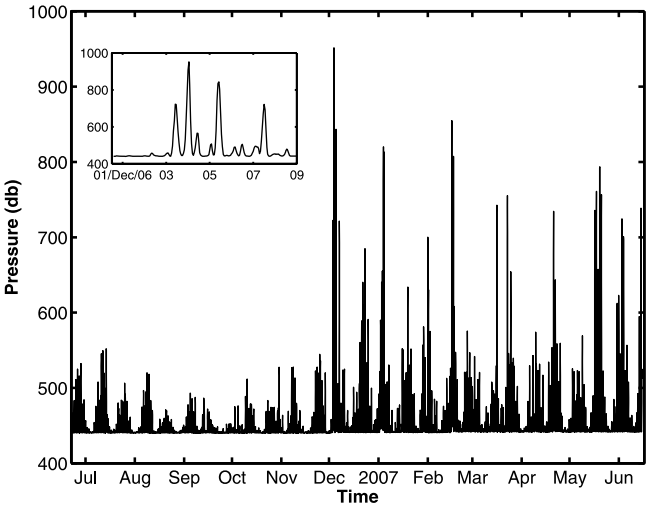

Figure 3. Pressure from the CTD positioned at about 440 m depth on the axis mooring 15 km from the mouth, over almost 1 year. The inset shows a zoom for the first 10 days of December 2006. The large-pressure variations, reaching up to 510 db, indicate mooring knockdown. There is a clear periodicity of about 2 weeks in the vertical displacements, reflecting the spring-neap cycle.

near the canyon center) suffered significant knockdown. The pressure recorded by the MicroCAT CTD nominally at 440 m on mooring SG11, revealed vertical displacements of up to 550 db (Figure 3). The moorings were designed for expected currents of 20–30 cm s^{-1}, but the actual currents far exceeded the design specification. Standard mooring models and bulk estimates of knockdown for the observed currents are consistent with the observed pressure changes (see auxiliary material).[1] Vertical shifts in the position of instruments poses a problem to the interpretation and analysis of the CTD and current meter data. Since the moorings SG10 and SG12 on the flanks of the Gully did not experience significant knockdown, the data there were unaffected. Note that the mooring SG12 on the western flank was within a feeder canyon.

[14] In order to produce a depth coherent data set, the following procedure was used to interpolate the data from the axis moorings to predetermined standard depths. The CTD measurements were used for temperature and salinity data, while the RCM8 and ADCP data on each mooring were used in combination to produce current velocities at the standard depths. The depth of every CTD was known precisely at each time from the recorded pressure. The depths of the RCMs and ADCPs at each time were calculated from the known depth of the closest CTD, and the known distance between instruments on the mooring, using geometry. This calculation assumed that the mooring remained taut, that is, that the distances separating instruments did not change with mooring knockdown. Once the depths of every instrument on a mooring had been determined, a linear interpolation was used to calculate the data on standard depths, positioned between the relevant instruments.

[15] Due to the differing nominal depths of CTDs and RCMs on each mooring, different standard depths were used for CTD and current velocity data. Further, because of differing instrument distribution, and the magnitude of knockdown, it was also required to use different standard depths for the two different moorings, SG2 and SG11. The standard depths for each mooring, and measurement type are given in Table 1. Data were interpolated to single standard depths for the full duration of the records (Table 1). These records, together with the records from moorings SG12 and SG10 shall be referred to as the full length records from here on. In order to retrieve information about the vertical variations in current velocity, a quiescent period of the records with minimal knockdown (18 June 2006 at 05:00:00 to 13 August 2006 at 06:00:00) was used to interpolate the current data to multiple standard depths (see Table 1). These will be referred to as the quiescent records.

[16] The measured sea level at Halifax and historical CTD data was obtained upon request from Integrated Science Data Management (ISDM) of the Department of Fisheries and Oceans, Canada. The historical CTD data incorporates all Temperature-Salinity profiles collected within 30 Nm of the Gully (43.91°N, 58.98°W) since 1970 and archived by ISDM. Further CTD data was collected during the mooring recovery cruise of the CCGS *Hudson* in August 2007 (Greenan et al., report in preparation, 2011). Hourly wind speed data for Sable Island concurrent with the mooring program were obtained from Environment Canada (http://www.climate.weatheroffice.ec.gc.ca).

[17] Several analysis procedures were applied to the available data. Power spectra for various time series were produced by applying a Hanning window and using the periodogram method [*Emery and Thomson*, 2001]. Confidence spectra for each of these were obtained by assuming a red noise background spectrum multiplied by the 95 percentile of the chi-square distribution [*Torrence and Compo*, 1998]. Harmonic analysis of the complex current velocities was conducted using the t_{tide} package [*Pawlowicz et al.*, 2002]. The tidal analysis provides the semimajor and semiminor axis, ellipse orientation and Greenwich phase, with confidence intervals, for the exact tidal constituent frequencies.

[18] In order to compute a measure of stratification, the potential density between vertically adjacent CTDs was subtracted to produce first differenced density time series at each of the moorings. Continuous Wavelet Transformations (CWT) [*Torrence and Compo*, 1998] were performed on complex current velocities, sea level at Halifax, wind speeds

Table 1. The Standard Depths (in m) to Which Data Was Interpolated[a]

	SG2		SG11	
Mooring	RCM	CTD	RCM	CTD
Full Record	750	500	800	400
Quiescent Record	350		265	
	500		375	
	700		560	
	900		1075	
			1520	

[a]Data was interpolated to a single standard depth (which differed by mooring and for current velocity/CTD) for the full time series. For a quiescent portion of the time series in July 2006, data was interpolated to multiple standard depths.

[1]Auxiliary materials are available in the HTML. doi:10.1029/2011JC006990.

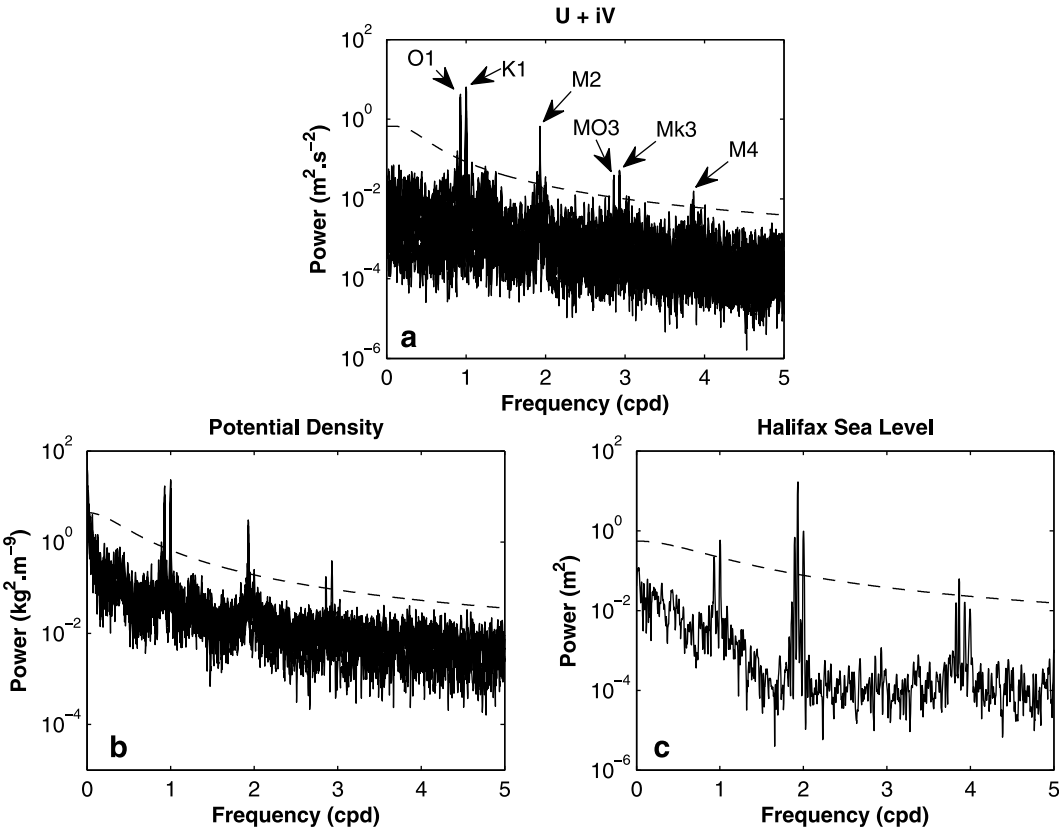

Figure 4. Fourier power spectra of (a) complex current velocities from the flank mooring RCMs and the full length interpolated velocities from the axis moorings, (b) the potential density computed from the all available CTDs, and (c) sea level from Halifax. The dashed lines give the 95% confidence spectra. Significant peaks at the tidal constituent frequencies are labeled in Figure 4a.

from Sable Island and first differenced density data. The Morlet wavelet was used as the basis function. In order to examine the temporal variability of power in the diurnal band, a scale average of wavelet power was produced for scales between 23 and 25 hours. For the Morlet basis function, wavelet scale is closely analogous to the Fourier period. The scale average is the weighted sum of wavelet power between the two scales and is equivalent to the average variance in the given band [*Torrence and Compo*, 1998].

3. Results

3.1. Mooring Observations in the Gully

[19] The vertical knockdown of moorings on the axis of the canyon already noted (Figure 3), provides some insight to the nature of processes operating in the Gully. In time, the magnitude of the maximum vertical displacements varied nearly sinusoidally with a period of around 2 weeks, suggestive of possible modulation by the spring-neap cycle. A magnification of the same pressure record for a 10 day period in December 2006 (Figure 3) reveals that individual displacements occurred with a periodicity of hours. For example, there were three clear peaks between 3 and 5 December. At monthly timescales there was an additional modulation of maximum displacements in time. The first half of the record between July and December was characterized by typical displacements of 100 db, while after peaking in December, displacements in the second half of the record had much larger maxima. Similar temporal modulation was evident in the current velocity and density records, to which we now turn.

[20] To objectively identify the dominant frequencies in the data records, power spectra were computed for all the full length complex current velocity and potential density time series, as well as for the sea level at Halifax (Figure 4). The Halifax sea level spectrum (Figure 4c), has its principal peak at the M_2 frequency. Secondary peaks occur at the S_2, M_4 and K_1 frequencies, in order of declining power. The ratio of the diurnal to semidiurnal amplitudes $K_1/M_2 = 0.19$. The sea level record indicates the dominance of the M_2 constituent of the barotropic tide in the region [*de Margerie and Lank*, 1986].

[21] The current velocity spectra from the Gully (Figure 4a) reveal a considerably different picture. The dominant spectral peaks are diurnal, at the K_1 and O_1 frequencies. The semidiurnal frequencies M_2, S_2, and the M_4 higher harmonic have significantly lower amplitudes than their diurnal counterparts. This is illustrated by the ratio of the amplitudes $K_1/M_2 = 3.12$. The sum frequencies $M_2 + K_1 = MK_3$ and $M_2 + O_1 = MO_3$, are statistically significant. The presence of these sum frequencies indicates a nonlinear interaction amongst the diurnal and semidiurnal tides, not evident in the sea level record. The potential density spectra (Figure 4b) are similar to the velocity spectra, except that the M4 constituent does not

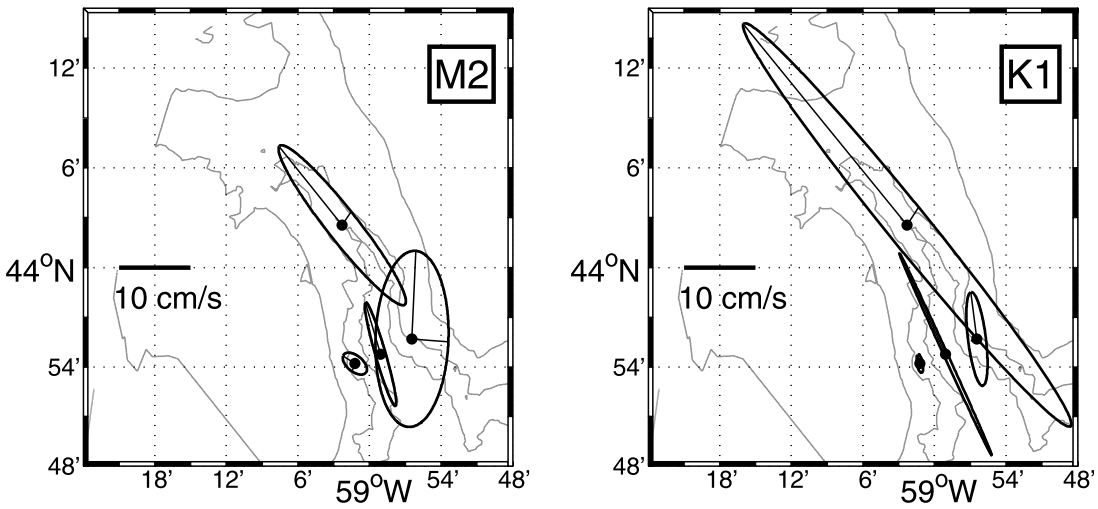

Figure 5. (left) M_2 and (right) K_1 tidal ellipses derived from harmonic analysis of the full length velocity records. The respective depths were 750 (head), 800 (center), 550 (western flank), and 316 m (eastern flank). The 200, 500, and 1000 m isobaths are contoured in gray.

appear as a significant peak. The correspondence between the density and velocity spectra, the appearance of the sum frequencies, and the shift to dominance of the diurnal constituents in the Gully records suggests that baroclinic motions are potentially important.

[22] To accurately characterize the nature of the tides in the full length velocity time series, harmonic analysis was applied to determine the ellipse information for the M_2 and K_1 frequencies (Figure 5). The semimajor axes of the M_2 ellipses at moorings near the head (SG2) and at the center (SG11) were well aligned with the axis of the canyon. The M_2 amplitude increased from the center (5.6 cm s^{-1}) toward the head (11.9 cm s^{-1}), where it was the largest. The mooring SG12 on the western canyon flank had a much lower M_2 amplitude than either mooring on the axis. The M_2 amplitude at SG10 on the eastern flank (8.9 cm s^{-1}) was larger than at the adjacent SG12 and SG11. This region of the eastern flank was where *Sandstrom and Elliot* [1984] reported energetic M_2 internal tides and solitons.

[23] The K_1 ellipses had a small magnitude on the flanks at SG12 and SG10, with the eastern flank again being the more energetic of the two. The K_1 semimajor axes in the canyon at moorings SG11 and SG2 were significantly larger than those on the flanks, and well aligned with the canyon axis. These K_1 ellipses were nearly rectilinear in the along-canyon direction, indicating minimal across-canyon flow at the K_1 frequency. The amplitude of the K_1 semimajor axis increased significantly from SG11 at the center (12.0 cm s^{-1}) toward SG2 at the head of the canyon (30.5 cm s^{-1}), where it was the largest.

[24] In order to gain some insight into the vertical structure of the tidal currents, harmonic analysis was again applied to the quiescent velocity records that included multiple standard depths. The ellipse information between the full length and quiescent records was in good agreement. Since the largest tidal currents (K_1) occurred on the axis of the canyon we focus our attention there. Vertical profiles of the amplitude of the semimajor axis of the tidal constituents at moorings SG2 and SG11 were derived from the quiescent records (Figure 6a). K_1 velocities were everywhere higher than those for M_2. At the central mooring SG11, the K_1 amplitude increased with depth from 7.3 cm s^{-1} at 265 m to 21.2 cm s^{-1} at 1520 m. The K_1 velocities near the head (SG2) were far higher than the central (SG11) velocities, and generally increased with depth, reaching a maximum of 35.0 cm s^{-1} at 700 m.

[25] The Greenwich phase gives the local response in relation to the tidal forcing at the reference longitude of the Greenwich Meridian. Larger phase angles correspond to a later arrival of the wave crests [*Pawlowicz*, 2002]. At both mooring SG2 and SG11, the phase of K_1 decreased with depth (Figure 6b). At the latter mooring, the phase change was 60° over the 1250 m shown. The observed phase change with depth is a further indication that the K_1 tide has a baroclinic component, since a purely barotropic tide would have equal phase at all depths. In the horizontal, the phase difference at K_1 between the moorings on the axis is close to zero. The moorings are separated by a distance of over 15 km, and the absence of a phase difference between them indicates a large horizontal wavelength ($\gg$15 km), or a standing wave pattern for K_1.

[26] The information gleaned from the harmonic analysis allowed the construction of a picture of the spatial variability of the major tidal constituents in the Gully. However it is clear from the earlier considerations of mooring knockdown that there is also significant temporal modulation of current velocities. In order to examine the temporal modulation of current velocity a continuous wavelet transformation (CWT) was performed on the full length velocity records. From these transformations, a scale average of wavelet power in the 23–25 h band was produced in order to consider the temporal modulation of diurnal current power. A principal component analysis of the diurnal current power time series of 8 RCMs, from the four moorings, results in only one significant principal component, that explains over 95% of the variance. Principal components two and above were not significant according to the Kaiser test [*Hsieh*, 2009]. The associated eigenvector was positive everywhere in space. The production of only one significant principal component with a uniformly positive eigenvector means that the

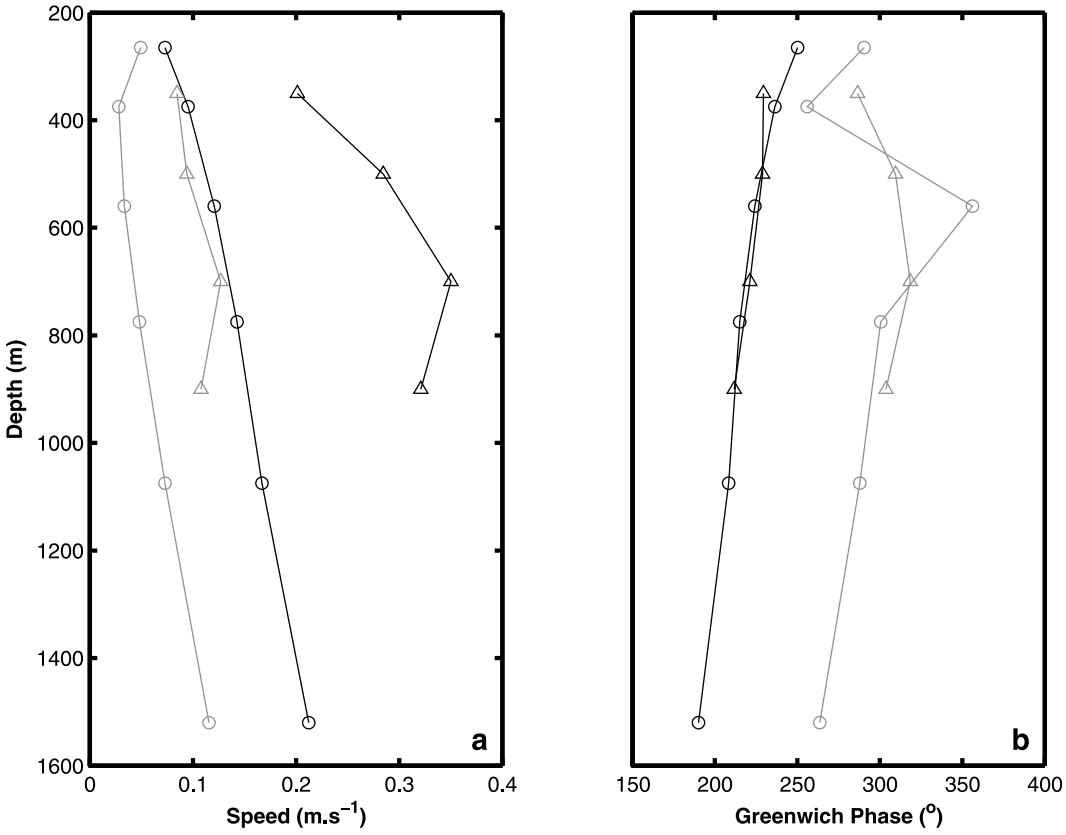

Figure 6. Vertical profiles of (a) major axis speed and (b) Greenwich phase, derived from harmonic analysis. Profiles are shown only for the moorings on the canyon axis, 15 (circles) and 30 km (triangles) from the mouth. Profiles for the K_1 tide are shown in black, and profiles for the M_2 tide are shown in gray.

modulation of diurnal current power was coherent in space. That is, the strength of the diurnal current velocity increased and decreased together at the four mooring locations. This then suggests that a single, region wide forcing mechanism was responsible for modulating the diurnal current speeds in the Gully.

[27] Several plausible mechanisms could alter the strength of the observed diurnal current, including wind speed, stratification (since baroclinic effects are anticipated) and the strength of barotropic tide. The first differenced potential densities between vertically adjacent standard depths are used as a proxy for the stratification, and the sea level at Halifax is considered a measure of the strength of the background barotropic tide. To the Halifax sea level we apply the CWT and scale averaging to produce a time series of diurnal barotropic power.

[28] A correlation matrix between diurnal current power, wind speed, stratification, and diurnal barotropic power was produced (Table 2). Only the barotropic power is significantly correlated with the diurnal current power. The modulation of diurnal current velocities is therefore principally controlled by the strength of the background barotropic tide.

[29] This relationship is elucidated by the observation that the diurnal barotropic power (solid line, Figure 7) and the diurnal current power (dashed line) varied together closely at the central mooring SG11. There was a distinct biweekly period set by the spring-neap cycle. Over monthly periods, the barotopic forcing and current velocity response also corresponded closely, as can be seen by smoothing the time series with a 27.5 day running mean (Figure 7, top). The large magnitude velocity response to barotropic forcing in the Gully indicates that resonance may have been occurring.

3.2. Models of Tidally Forced Flow in a Canyon

3.2.1. Basic Model Configuration

[30] The mooring observations from within the Gully revealed that diurnal tidal currents were far stronger in the centre of the canyon, where they were rectilinear and directed along the canyon axis. Numerical tidal models of the Scotian Shelf [e.g., *de Margerie and Lank*, 1986; *Gordon and Fenton*, 2002] show that the K_1 tidal ellipses are generally orientated

Table 2. Correlation Between Low-Frequency Diurnal Current Power and Barotropic Forcing, Stratification, and Wind Speed[a]

RCM K_1	Hsl K_1	Δ Density	Wind Speed
1.000	**0.902**	−0.197	0.172
0.902	**1.000**	−0.370	0.192
−0.193	−0.370	**1.000**	0.040
0.172	0.192	0.040	**1.000**

[a]The correlation matrix is between scale averaged diurnal power from the central RCM velocities (RCM K_1), scale averaged diurnal power from Halifax sea level (Hsl K_1), the first differenced density between two vertically adjacent CTDs (Δ Density) and wind speed from Sable Island (Wind Speed). All fields, originally at hourly resolution, were smoothed with a 27.5 day running mean before the correlations were computed. Statistically significant (5%) correlations are shown in bold.

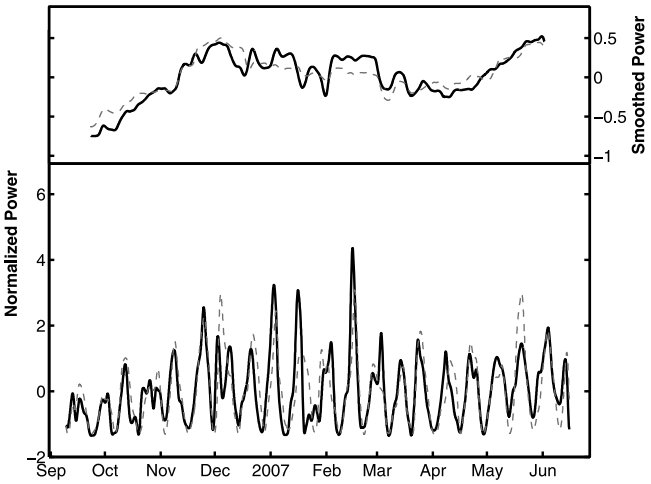

Figure 7. (bottom) Scale-averaged power for the diurnal (23–25 h) band from Continous Wavelet Transformations. The dashed line represents diurnal power from the complex velocities from the central mooring at 750 m. The solid black line represents diurnal power from Halifax sea level. (top) The same power time series that have been smoothed with a 27.5 day running mean. Only data from mid-September 2006 onward were used due to missing values in the sea level record.

along the shelf, with typical velocities of 5–10 cm s^{-1}. The model of *de Margerie and Lank* [1986] showed elevated K_1 and O_1 velocites on the flanks of The Gully. Within the canyon, the numerical models do not produce the strong, along-canyon (and therefore across shelf) velocities that are observed. The purpose of this section is to develop a dynamical framework that is capable of explaining the along-canyon diurnal flow in the Gully, with the observed pattern of amplification toward the axis and the head. We do this by developing two separate, yet complementary analytical models. The first (section 3.2.2) establishes the influence of a uniform trench like topography on the baroclinic response to overhead barotropic flow. The second model (section 3.2.3) aims to capture the sensitivity of the along-canyon velocity structure to geometric changes in that direction (i.e., to the narrowing and shoaling of the canyon toward the head). In both cases, as a simple first approximation that permits analytical consideration, the vertical structure will be represented as a 1.5 layer system.

[31] In reality, the potential density section (Figure 8) shows that potential density increases rapidly with depth in the upper 200 m. Between 200 and 2000 m, the density increase is nearly linear, and far smaller in magnitude, resulting in a near constant buoyancy frequency. We do not represent this continuous stratification, but use a typical value of the buoyancy frequency to inform the selection of the reduced gravity, g', in our 1.5 layer system. This is done by requiring the Rossby radius to remain consistent through both representations. In the continuously stratified case, $R = c/f$, where c is the wave speed. Using vertical density profiles it is possible to calculate the speed, c, of a mode one wave over a flat bottom, and the corresponding Rossby radius. The average of the black profiles in Figure 8 yields $R = 14$ km. One standard deviation on either side of the mean profile results in the range, $22 > R > 2.5$ km. In the 1.5 layer system the Rossby radius, $R = \sqrt{g'h}/f$. The choice here is for the lower-layer thickness, $h = 1600$ m, so that the interface lies 100 m above the depth of the shelf surrounding the canyon (see section 1.2). To have $R = 14$ km the appropriate value of g' is about 1.2×10^{-3} m s^{-2} in our 1.5 layer system. However the specific values adopted for g', and the corresponding R values are model dependent and are given by section below.

[32] The linear, rotating, inviscid, Boussinesq, shallow water momentum equations for the baroclinic flow in the lower layer are [*Gill*, 1982]

$$\frac{\partial u}{\partial t} - fv = -g'\frac{\partial \eta}{\partial x}, \qquad \frac{\partial v}{\partial t} + fu = -g'\frac{\partial \eta}{\partial y} \tag{2}$$

here u is the across-channel velocity, f is the Coriolis frequency, v is the along-canyon velocity, and η is the elevation of the interface between the two layers. Here we have made the further approximation of a 1.5 layer system by letting the depth of the upper layer go to infinity and assuming the baroclinic velocities there to be zero. In the following sections an appropriate form of the conservation of mass is adopted, and the two models are developed.

3.2.2. Double Kelvin Wave Model of Flow Over an Infinite Trench

[33] Here we are interested in the lower-layer baroclinic response to a background barotropic forcing, in the presence of topography. Topographic variations in y are neglected,

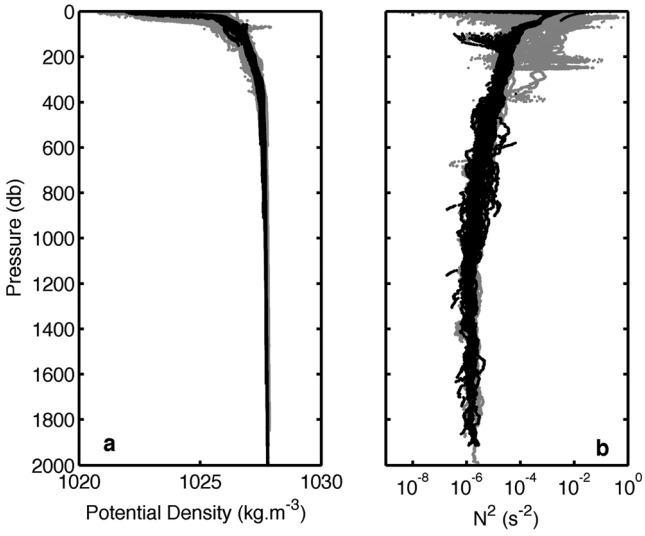

Figure 8. Vertical profiles of (a) potential density and (b) buoyancy frequency from the Gully region. The black points denote data collected during mooring recovery operations in the Gully during August 2007. N^2 profiles have been smoothed. The gray points denote historical data, within a 30 Nm radius of the central mooring, collected since 1970 and retrieved from the ISDM archive. All months between March and December are represented in the historical data, but the majority of stations were occupied in July–October and few stations were occupied in November–December.

and the flow assumed to be uniform in that direction. The conservation of mass in the lower layer is

$$\frac{\partial \eta}{\partial t} + \frac{\partial (hu)}{\partial x} = 0 \tag{3}$$

where h is the thickness of the lower layer. Variations of canyon geometry across shelf are not considered here for simplicity, but are dealt with later. Thus, the model is appropriate for considering uniform along-shelf flow that encounters an infinitely long trench. With these assumptions we arrive at the simplified expression for forced flow over topography [*Allen and Thomson*, 1993]

$$g'h\frac{d^2u}{dx^2} + 2g'\frac{dh}{dx}\frac{du}{dx} - \left(f^2 - \omega^2\right)u = -g'\frac{d^2h}{dx^2}(u_0 + u) \tag{4}$$

here ω is the forcing frequency, and u_0 is the velocity of the across-trench background barotropic forcing. Time dependence has been removed by assuming that the forcing and the baroclinic response, $(u_0, u) \propto e^{i\omega t}$. The key aspect of the dynamics of this system is that the cross-trench barotropic flow u_0, forces an along-trench baroclinic response, v in the lower layer. This uniform along-trench perturbation velocity is stronger than the cross-trench perturbation velocity and from (2)

$$v = -\frac{f}{i\omega}u \tag{5}$$

[34] The perturbation velocity u is related back to the total velocities and interface displacement by [*Allen and Thomson*, 1993]

$$\begin{aligned} U &= (u_0 + u)e^{i\omega t} \\ V &= \left(v_0 - \frac{f}{i\omega}u\right)e^{i\omega t} \\ \eta &= -\frac{1}{i\omega}\left(h\frac{du}{dx} + \frac{dh}{dx}[u_0 + u]\right)e^{i\omega t} \end{aligned} \tag{6}$$

[35] The simplest case of a rectangular trench of width W and depth ΔH, centered on $x = 0$ (Figures 9a and 9c) may be solved analytically. Separate solutions can be found within the trench, and far from the trench, where $dh/dx = 0$, and the expression for the perturbation velocity simplifies to

$$g'h\frac{d^2u}{dx^2} - \left(f^2 - \omega^2\right)u = 0 \tag{7}$$

[36] The condition within the trench is that the flow is symmetrical, requiring $\partial u/\partial x = 0$ at $x = 0$. The solution is

$$u = C\cosh(x/R'_\omega) \tag{8}$$

[37] The term $R'_\omega = (g'\,(H_0 + \Delta H)(f^2 - \omega^2)^{-1})^{1/2}$ is the deformation radius for oscillating flow within the trench, where H_0 is the depth of the bottom layer over the shelf.

[38] On the shelf, far from the trench the solution is

$$u = Ae^{-|x|/R_\omega} \tag{9}$$

where the condition that the perturbation velocity must remain bounded as $x \to \infty$ has been applied. Here $R_\omega = (g'H_0\,(f^2 - \omega^2)^{-1})^{1/2}$ is the deformation radius for oscillating flow on the shelf, away from the trench. At the edge of the trench, $x = W/2$, these two solutions must match, providing the values of the constants A and C. The conditions governing the solutions at the edge of the trench are that the interface displacement, η must be continuous, to ensure finite velocities, and the total cross-trench mass flux must also be continuous.

[39] The solution for a rectangular trench with a width $W = 2.5\,R$, where the lower-layer depth, $h = H_0 = 200$ m, is defined over the shelf yielding $R = 1.5$ km, $g' = 1 \times 10^{-4}$ m s^{-2}, a trench depth $\Delta H = 0.5H_0$ and a forcing frequency $\omega/f = 0.6$ is similar but opposite to the top hat ridge solution [*Allen and Thomson*, 1993]. However note that the along-canyon velocity is shown here, while *Allen and Thomson* [1993] showed the cross-canyon velocity (Figure 9a). The magnitude of the maximum velocities within the trench are about half those for the corresponding ridge. The positive phase of the barotropic forcing drives a baroclinic response v, that is positive inside the trench, and an oppositely directed response outside of the trench. It is worth noting that (5) implies that the across-trench perturbation velocity u is out of phase with the barotropic forcing u_0. This means that within the trench the total across-trench velocity U is reduced by the baroclinic response, while outside of the trench it is enhanced. This solution applies only for subinertial frequencies. Superinertial barotropic flow over the trench will also generate a response, although it takes on the form of an oscillatory standing wave. The along-trench flow will also be reduced relative to the forcing for superinertial frequencies according to (5), since in this case $\omega > f$.

[40] For a more realistic triangular trench profile, with a slope $s = \Delta H/(W/2)$, the solution is obtained numerically by using a 'shooting method' [*Allen and Thomson*, 1993]. The velocity outside of the trench is again negative, but considerably smaller than in the rectangular case (Figure 9b). The important feature to note is that the along-canyon perturbation velocity increases toward the center of the trench with the triangular profile. Solutions are also shown for the two trench profiles using parameters similar to those observed in The Gully (Figures 9c and 9d). Specifically, $W = R = 14$ km, where the lower-layer depth $h = H_0 + \Delta H = 1600$ m is defined over the trench, $g' = 1.2 \times 10^{-3}$ m s^{-2}, the trench depth $\Delta H = 15H_0$ and $\omega/f = 0.73$.

[41] The maximum along-canyon velocity in the center of the triangular trench depends on the width of the trench relative to the Rossby radius, W/R, the trench depth relative to the lower-layer depth on the shelf, $\Delta H/H_0$ and the forcing frequency relative to the Coriolis frequency, ω/f (Figure 10). Narrower trenches have more rapid along-trench velocities (10a). Thus as noted above, the total across-trench velocity, U, decreases with narrowing trench width, as expected. The perturbation velocity also increases as the forcing frequency approaches the local inertial frequency (Figure 10a and 10b). Increasing trench depth (Figure 10b) has an intriguing effect. Deeper trenches have more rapid along-trench perturbation velocities. As the barotropic flow crosses the edge of the trench, the depth increases, generating cyclonic relative vorticity. On exiting the trench, the flow is compressed

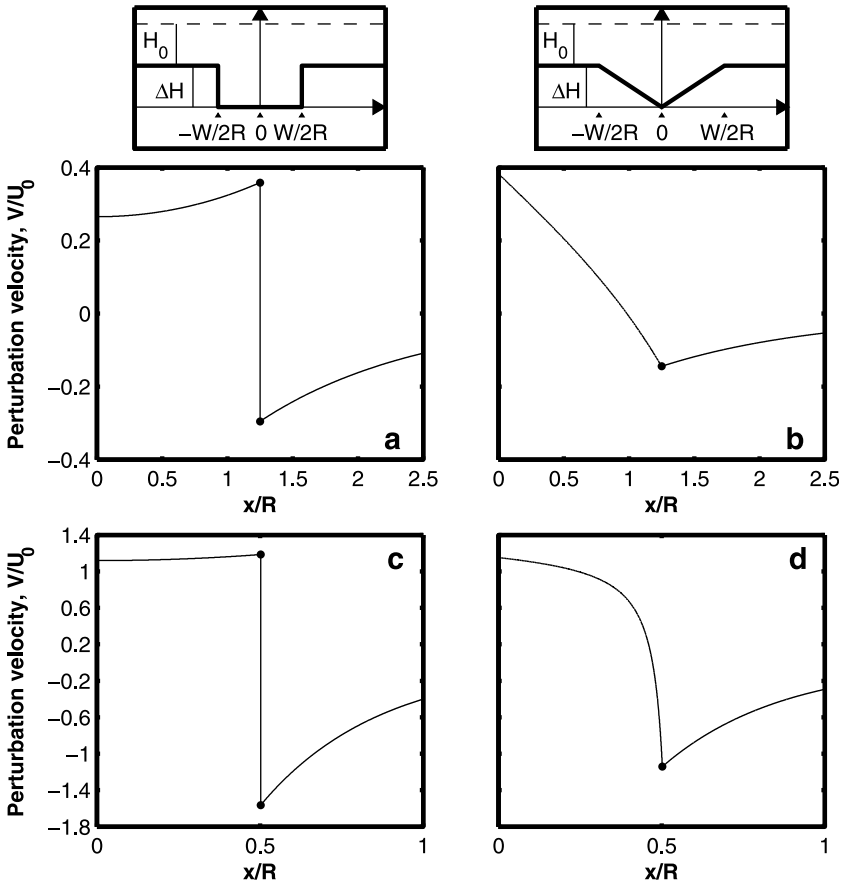

Figure 9. Perturbation velocities in the along-trench direction from the 1.5 layer model. (a) Analytic solution for a rectangular trench with $W = 2.5R$, $H_0 = 2\Delta H$, and a reduced gravity $g' = 1 \times 10^{-4}$ m s^{-2}; (b) numeric solution for a triangular trench profile with the same parameters as in Figure 9a; (c) analytic solution for a rectangular trench with parameters similar to the Gully, $W = R$, $H_0 = 0.07\Delta H$ and $g' = 1.2 \times 10^{-3}$ m s^{-2}; and (d) numeric solution for a triangular trench with the same parameters as in Figure 9c. The profiles of the rectangular and triangular trench are shown on top. Figures 9a and 9c are the corresponding trench solutions to the top hat and triangular ridges of *Allen and Thomson* [1993], except that the along-trench velocities are shown here.

and accelerates, generating anticyclonic vorticity. The net response is therefore a standing double Kelvin wave over the trench which is uniform along the homogeneous topography in y.

3.2.3. Canyon Seiche Model

[42] The 1.5 layer model in the previous section established that across-canyon barotropic flow would drive an along-canyon baroclinic velocity of the same order. How-

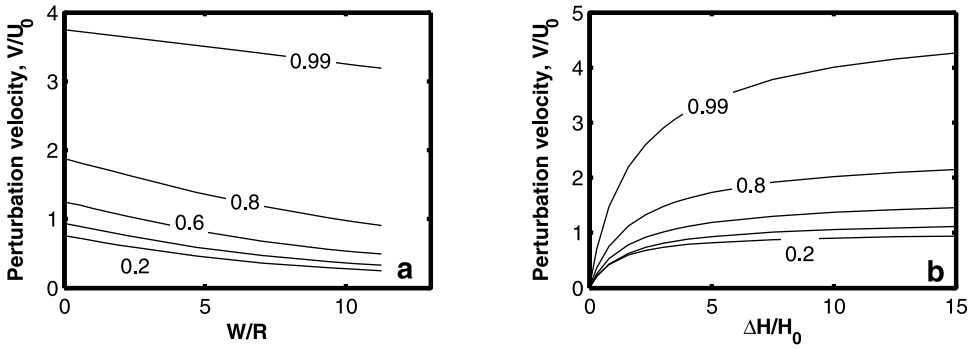

Figure 10. Parameter spaces for the 1.5 layer model of a triangular trench. (a) Perturbation velocity as a function of trench width W/R, for various values of ω/f between 0.2 and 0.99. The trench depth is $\Delta H/H_0 = 3$. (b) Perturbation velocity as a function of trench depth, $\Delta H/H_0$, for various values of ω/f. The trench width is $W = 2.5R$. All perturbation velocities are given at the center of the trench.

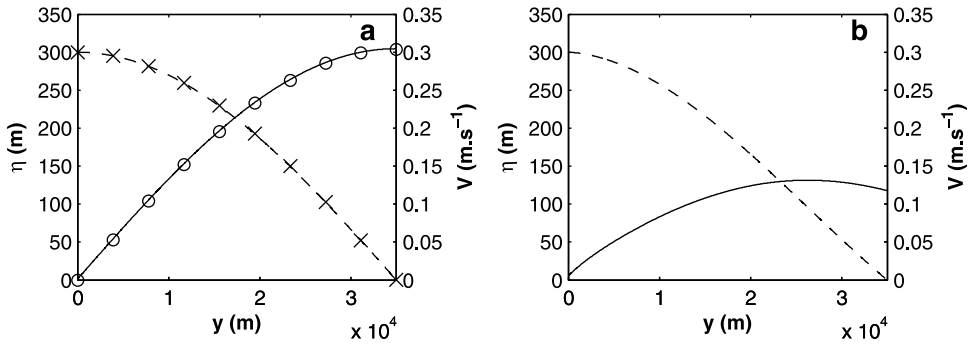

Figure 11. Interface height (dashed) and along-canyon velocity (solid) for the gravest mode of resonance in a canyon with constant along-axis depth shown for (a) a canyon of constant width (the circles and crosses show the analytical solution) and (b) a canyon that narrows to a width $W_{head} = 1/10 W_{mouth}$. In both Figures 11a and 11b the canyon length is $L = 35$ km and interface displacement is $\eta = 300$ m at the head; reduced gravity is $g' = 1.65 \times 10^{-3}$ m s^{-2} in Figure 11a; and reduced gravity is $g' = 8.40 \times 10^{-4}$ m s^{-2} for resonance in Figure 11b. The open ocean is at $y = 35$ km, where the boundary condition $\eta = 0$ m, and the canyon head is at $y = 0$ km, where the boundary condition is $v = 0$ m s^{-1}.

ever, the model was for an infinite trench, and did not consider variations in the along-canyon direction. We address this now by considering along-axis flow in a 1.5 layer channel of length L in the y direction, with a closed boundary at the head ($y = 0$). The completely closed boundary condition at the head conflicts with our statement that the density interface lies 100 m above the canyon rim (section 3.2.1). We address the effect of differing boundary conditions at the head later. For the case where the narrow channel approximation holds, it can be assumed that the across-canyon velocities are negligible [*Gill*, 1982], so that

$$fv = g' \frac{\partial \eta}{\partial x}, \qquad \frac{\partial v}{\partial t} = -g' \frac{\partial \eta}{\partial y} \tag{10}$$

The along-canyon flow will be in geostrophic balance with a cross-canyon interface tilt. We assume the velocity is uniform across the canyon. For a channel with a variable width W, and lower-layer depth H, the conservation of mass in the along-canyon direction (y) is given by [*Gill* 1982, p. 113]

$$W(y) \frac{\partial \eta'}{\partial t} + \frac{\partial A v}{\partial y} = 0 \tag{11}$$

where the cross-sectional area at any point along the channel is given as $A = WH$, and η' is the on axis interface displacement. Substitution of the y momentum equation (10) into (11) gives

$$W \frac{\partial^2 \eta}{\partial t^2} = g' \frac{\partial}{\partial y} \left[A \frac{\partial \eta}{\partial y} \right] \tag{12}$$

This equation describes the flow along a channel with a closed head and a variable geometry in y. For the simplest geometric case of constant W and H and by applying a zero impedance condition at the open mouth, an analytic solution can be found for (12) [*Gill*, 1982]. In this analytic case, the wavelengths and associated frequencies of permitted oscillations in the channel are limited to the discrete set

$$kL = \left(n + \frac{1}{2} \right) \pi \tag{13}$$

and

$$\frac{\omega L}{c} = \left(n + \frac{1}{2} \right) \pi \qquad \text{for n} = 0, 1, 2 \ldots \tag{14}$$

These are the familiar resonant frequencies for the channel, and the lowest mode, $n = 0$, describes the channel seiche with a wavelength $4L$. The wave speed $c^2 = g'H$. The forcing frequency $\omega = 7.27 \times 10^{-5}$ s^{-1} is diurnal, and the reduced gravity $g' = 1.65 \times 10^{-3}$ m s^{-2} (and thus c) was selected so to as to make the channel resonant. The corresponding Rossby radius is 16 km. The velocity solution (Figure 11a, circles) shows that the along-canyon velocity is highest at the mouth, and reduces rapidly to zero as the solid vertical wall at the head of the canyon is approached. By contrast, the interface displacement is greatest at the head of the channel, and zero at the mouth, consistent with the zero impedance condition (Figure 11a, crosses). It can also be seen that a numerical solution to the equations (Figure 11a, solid lines), exactly matches the analytical solution in this example.

[43] In the more general case of variable geometry, the quarter wavelength channel seiche also occurs, but the nature of the along-canyon velocity and interface displacement differ depending on the exact geometric changes. The details of the along-canyon distribution of v and η can be determined numerically for any geometry from (12).

[44] We select to first consider the case of a flat bottomed canyon, that narrows toward the head. The width at the head is chosen so that $W_{head} = 1/10 W_{mouth}$. For resonance with the narrowing geometry, $g' = 8.4 \times 10^{-4}$ m s^{-2}. The along-canyon velocities (Figure 11b) in this case are generally lower, due to the lower g' required to make the channel resonant. However note that the magnitude of the velocities shown here are for an arbitrarily selected isopycnal displacement of 300 m at the canyon head. We are primarily concerned with the pattern of the velocity, which is unaffected by the selection of interface displacement. In particular, for the narrowing canyon case, the maximum velocity occurs closer to the head (26 km; Figure 11b) than in the constant width case (35 km; Figure 11a).

[45] Another possible geometrical change is a shoaling of depth toward the head of the canyon. To investigate the

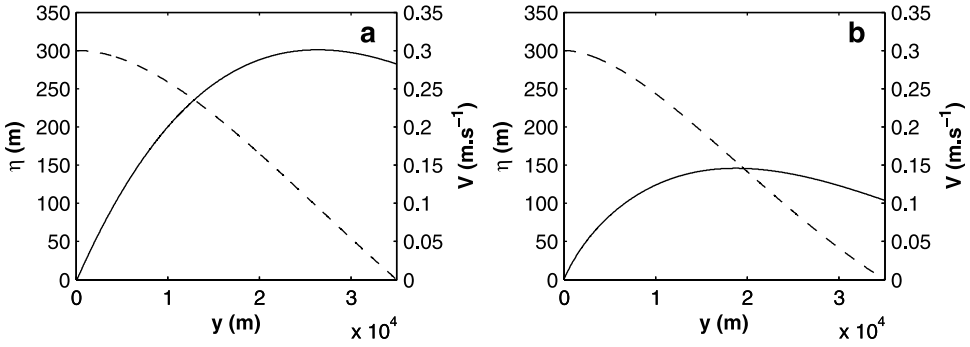

Figure 12. Interface height (dashed) and along-canyon velocity (solid) for the gravest mode of resonance in a canyon with a shoaling depth for (a) a canyon of constant width and (b) a canyon that narrows to a width $W_{head} = 1/10W_{mouth}$. In both cases the canyon shoals to $H_{head} = 1/2H_{mouth}$, the canyon length is $L = 35$ km and interface displacement is $\eta = 300$ m at the head; reduced gravity is $g' = 1.95 \times 10^{-3}$ m s^{-2} in Figure 12a; and reduced gravity is $g' = 1.0 \times 10^{-3}$ m s^{-2} for resonance in Figure 12b. The open ocean is at $y = 35$ km, where the boundary condition $\eta = 0$ m, and the canyon head is at $y = 0$ km, where the boundary condition is $v = 0$ m s^{-1}.

influence of shoaling depth on the along- canyon velocity field, we consider the case where $H_{head} = 1/2H_{mouth}$. First, the case of a constant width canyon, with a shoaling bottom is considered (Figure 12a). Here for the channel to be resonant, we determine a value of g' numerically, since no analytical solution exists for the sloping bottom case. We do this by requiring the boundary condition, $v = 0$, be met at the head of the canyon, and this is achieved for $g' = 1.95 \times 10^{-3}$ m s^{-2}. The shape of the velocity profile is changed from the flat-bottomed case (Figure 11a). At midcanyon, 20 km from the head, the velocities are higher when the canyon has a shoaling bottom. If the effect of bottom shoaling, and narrowing are considered together, the velocity profile is considerably modified (Figure 12b). Here $g' = 1.0 \times 10^{-3}$ m s^{-2} for resonance, again a value determined numerically. The no flow condition through the solid wall at the head still requires the velocity to be zero there. However, the maximum velocity occurs 19 km from the canyon head, and decreases toward the mouth. These numerical results demonstrate that along-canyon changes in geometry have the ability to significantly alter the velocity profile of a resonant wave within the canyon.

4. Discussion

[46] The observation that the K_1 tide dominates the Gully is highly unusual. Previous studies of canyons at similar latitudes have unanimously shown the highest tidal velocities occur at the M_2 frequency [*Hotchkiss and Wunsch*, 1982; *Petruncio et al.*, 1998; *Kunze et al.*, 2002; *Wang et al.*, 2008; *Lee et al.*, 2009]. The explanation of enhanced M_2 tidal velocities has concentrated on geometric focusing of the free M_2 internal tide by supercritical canyon topography [*Hotchkiss and Wunsch*, 1982] and local in-canyon generation on critical bottom slopes [*Petruncio et al.*, 2002]. However, these mechanisms are both unable to explain the amplification of the bottom-trapped K_1 tide in the Gully.

[47] The proceeding sections developed two models for describing the nature of oscillatory flow in a canyon. We now draw these models together, and attempt to explain the observed velocity structure in the Gully. Diurnal barotropic tidal flows on the Scotian shelf are generally orientated along the shelf [*de Margerie and Lank*, 1986; *Gordon and Fenton*, 2002]. Following section 3.2.2, we anticipate that in the presence of stratification, an along-shelf barotropic tide will force a cross-shelf baroclinic velocity in the lower layer of a canyon. The strength of the baroclinic response depends on given geometrical features of the canyon.

[48] In the Gully, the canyon width (<15 km) is approximately the same as or less than the observed mean Rossby Radius (14 km; see 3.2.1). The ratio of lower-layer depth over the canyon, to the lower-layer depth over the shelf, $\Delta H/H_0$, varies along the length of The Gully (see section 1.2; Figure 8), but generally $\Delta H/H_0 > 5$. At the latitude of the Gully (44°N), the diurnal forcing frequency is subinertial ($\omega = 7.27 \times 10^{-5}$ s^{-1}), yet it is approaching that of the local inertial frequency ($f = 1.01 \times 10^{-4}$ s^{-1}). The across-canyon geometrical profile of the Gully is nearly triangular, suggesting that the model developed in section 3.2.2 can appropriately be applied. The baroclinic response in v at the center of the canyon for the set of geometrical parameters representing the Gully is found to be on the same order as the barotropic forcing for these near diurnal frequencies (Figure 9d). Superinertial tides such as M_2, will also excite a baroclinic response in The Gully, although its magnitude will be less than the barotropic forcing.

[49] The nature of the velocity profile in the along-canyon direction again depends on the canyon geometry, the forcing frequency, and the strength of the stratification. The Gully represents a special case in this regard. The diurnal frequency is very near to resonant for the observed stratification. For quarter wavelength resonance in a flat bottomed channel, the required constraints on the channel length and stratification are given by equation (14). For $\omega L/c = 0.5\pi$ requires $R = 16$ km, close to the observed mean value. Indeed, it has been proposed that much of the Scotian shelf is resonant with respect to the diurnal tide [*Gordon and Fenton*, 2002]. A resonant wave in a canyon conforms to the framework established in section 3.2.3. An idealized canyon with a narrowing ($W_{head} = 1/10W_{mouth}$) and shoaling ($H_{head} = 1/2H_{mouth}$) geometry corresponding to the Gully (see section 1.2), has an along-canyon velocity profile as given by Figure 12b.

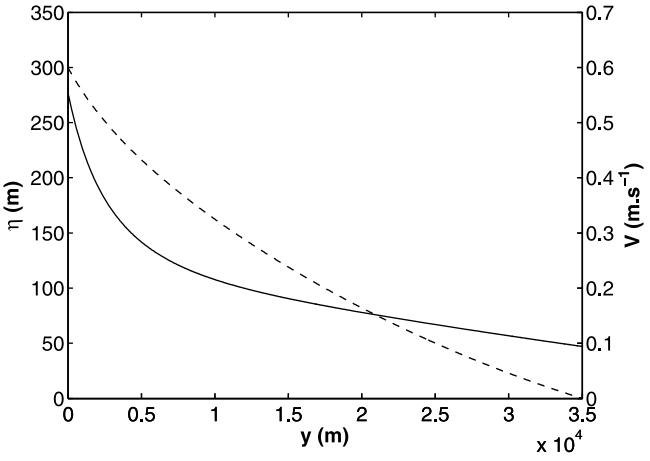

Figure 13. Interface height (dashed) and along-canyon velocity (solid) for the gravest mode of resonance in a canyon with a shoaling depth and open boundary condition at the head. The canyon narrows to a width $W_{head} = 1/10 W_{mouth}$. The canyon shoals to $H_{head} = 1/2 H_{mouth}$, the canyon length is $L = 35$ km, interface displacement is $\eta = 300$ m at the head, and reduced gravity is $g' = 1.65 \times 10^{-3}$ m s^{-2}. The open ocean is at $y = 35$ km, where the boundary condition $\eta = 0$ m, and the canyon head is at $y = 0$ km, where the boundary condition is $v = 0.57$ m s^{-1}.

The velocity maximum 19 km from the head is approximately 1.6 times greater than the velocity at the mouth. The role of the resonance is then to successively amplify the effects of the geometric funneling on the along-canyon baroclinic flow. This resonance for near diurnal frequencies in The Gully is responsible for the dominance of the K_1 and O_1 currents that we observed (section 3.1), despite the fact that the barotropic forcing is greater at the M_2 frequency.

[50] How do these simple model projections of the velocity profile in the Gully compare to the observations? The observed currents (section 3.1) were nearly rectilinear in the along-canyon direction. This is consistent with the prediction in section 3.2.2 that the baroclinic response acts to reduce the total across-canyon velocity U. The narrow-channel approximation adopted in section 3.2.3 follows directly. In the vertical, the observed currents within the Gully intensified with depth. This is expected since poleward of 30°, where the local inertial frequency exceeds 7.29×10^{-5} s^{-1}, forced motions at the diurnal frequency and below are bottom trapped [*Gill*, 1982]. This fact supports our use of a 1.5 layer model to examine the baroclinic velocities in the lower layer only.

[51] Spatially, the observations suggested a pattern of minimal velocities at the edges of the canyon, with the maximum along-canyon velocity near the axis (Figure 5). The double Kelvin wave model using a triangular geometry (Figure 9d) predicts this increase in the v velocity to a maximum at the center of the canyon. At the canyon rim, the predicted velocity is also small, as in the observations. Thus, the Kelvin wave model accurately predicts the spatial velocity pattern in the across-canyon direction.

[52] In the along-canyon direction, the mooring observations showed an approximate doubling in velocities from the central mooring SG11, to the mooring around 5 km from the head of the canyon (Figures 5 and 6). The canyon seiche model (section 3.2.3) dealt with the along-canyon velocity profile. The model prediction for a shoaling and narrowing canyon (Figure 12b), was for an 1.5 × increase in current speed from the mouth of the canyon to the maximum around 19 km for the head, after which it decayed to zero. The assumption of a vertical wall at the head of the canyon, which forces the model velocity to zero may be unnecessarily limiting.

[53] While something resembling a vertical wall does occur in the Gully (Figure 2d, at 0 km), it does not reach to the surface. In all likelihood, some of the fluid resonating within the canyon spills over onto the surrounding shelf. We can more fully incorporate this process by changing the model boundary condition at the head of the canyon. The choice of the velocity open boundary condition at the canyon head is subjective. As an example we consider the case where 10% of the volume entering the canyon at the mouth is spilt onto the shelf through a 100 m thick, 2 km wide layer at the canyon head. The volume entering the canyon is taken to be the K_1 velocity 0.12 m s^{-1}, multiplied by the cross-sectional area (9.6×10^6 m^3) at mooring SG11 (see section 3.1). The resulting estimate of the velocity boundary condition at the canyon head is 0.57 m s^{-1}, and we use this to numerically determine $g' = 1.65 \times 10^{-3}$ m s^{-2} in order for resonance at the diurnal frequency, when stipulating an isopynal displacement of 300 m at the head. The model velocity profile under the new boundary condition shows a monotonic increase in velocity toward the head (Figure 13). The velocity 5 km from the canyon head (0.28 m s^{-1}) is almost twice that 20 km from the head (0.16 m s^{-1}). This then matches the observed doubling of velocities between the moorings SG11 and SG2, in the Gully (section 3.1). The magnitude of the velocity profile shown here is dependent on our subjective choice of the velocity boundary condition at the canyon head, but the pattern of monotonic velocity increase toward the head is robust for any reasonable choice.

[54] For our informed choice of boundary conditions, the model produces velocity magnitudes within 0.04 m s^{-1} of the observed K_1 velocities. There is excellent qualitative agreement between the predicted along-canyon velocity profile and the observations. The enhanced nutrient availability and gross primary production at the head of the Gully has been suggested to support the high concentrations of demersal fish and cetaceans observed in The Gully MPA. The increase in tidal seiche velocities toward the canyon head, as simulated here, provides a mixing mechanism to explain the elevated nutrient [*Strain and Yeats*, 2005] and organic carbon [*Gordon and Fenton*, 2002] concentrations observed.

[55] The models presented here are extreme simplifications and cannot be expected to capture all the dynamics occurring in the Gully. The models assumed a smoothly oscillating barotropic forcing, that had only an alongshore component. The true details of the barotropic tide on the Scotian Shelf are poorly known, but likely to be more complex. We have argued above that the bottom trapped nature of the diurnal oscillations validates the choice of a 1.5 layer model. However, the actual stratification is continuous (Figure 8) and able to support higher modes. The model topographies are also extremely idealized. In the real Gully, a complex interaction between the topography and the continuous stratification generates a diversity of internal

waves and solitons [*Sandstrom and Elliot*, 1984]. The 1.5 layer, linear models cannot represent these processes. Since the models are also inviscid, they do not represent the dissipation and mixing resulting from internal waves. Despite these evident limitations, the excellent agreement between the predicted and observed velocity structure in the Gully suggests that we have succeeded in representing the most important processes in our simple dynamical framework.

[56] **Acknowledgments.** N.C.S. was supported by the National Research Foundation, South Africa; the University of British Columbia; and a NSERC Discovery grant to S.E.A. We thank the crew of CCGS *Hudson*, the technical operations group at BIO, and the DFO Oceans Branch (Maritimes Region) for providing financial support for the field program.

References

Allen, S., and X. Durrieu de Madron (2009), A review of the role of submarine canyons in deep-ocean exchange with the shelf, *Ocean Sci.*, *5*, 607–620.

Allen, S., and R. Thomson (1993), Bottom-trapped subinertial motions over midocean ridges in a stratified rotating fluid, *J. Phys. Oceanogr.*, *23*, 566–581.

Baines, P. (1983), Tidal motion in submarine canyons—A laboratory experiment, *J. Phys. Oceanogr.*, *13*, 310–328.

Boyer, D., D. Haidvogel, and N. Pérenne (2004), Laboratory–numerical model comparisons of canyon flows: A parameter study, *J. Phys. Oceanogr.*, *34*, 1588–1609.

Cacchione, D., and D. Drake (1986), Nepheloid layers and internal waves over continental shelves and slopes, *Geo-Mar. Lett.*, *6*, 147–152.

Cacchione, D., L. Pratson, and A. Ogston (2002), The shaping of continental slopes by internal tides, *Science*, *296*, 724–727.

Carter, G. S., and M. C. Gregg (2002) Intense, variable mixing near the head of monterey submarine canyon, *J. Phys. Oceanogr.*, *32*(11), 3145–3165.

de Margerie, S., and K. Lank (1986), Tidal circulation of the Scotian Shelf and Grand Banks, *Can. Contract. Rep. Hydrogr. Ocean Sci. 21*, ASA Consult., São Paulo, Brazil.

Emery, J., and R. Thomson (2001), *Data Analysis Methods in Physical Oceanography*, 2nd ed., Elsevier, Amsterdam.

Gill, A. (1982), *Atmosphere-Ocean Dynamics*, *Int. Geophys. Ser.*, Vol. 30, Academic, San Diego, Calif.

Gordon, D., and D. Fenton (2002), Advances in understanding the Gully ecosystem: A summary of research projects conducted at the Bedford Institute of Oceanography (1999–2001), *Can. Tech. Rep. Fish. Aquat. Sci. 2377*, Bedford Inst. of Oceanogr., Dartmouth, N. S., Canada.

Gordon, R., and N. Marshall (1976), Submarine canyons: Internal wave traps?, *Geophys. Res. Lett.*, *3*(10), 662–624.

Han, G., and J. W. Loder (2003), Three-dimensional seasonal-mean circulation and hydrography on the eastern Scotian Shelf, *J. Geophys. Res.*, *108*(C5), 3136, doi:10.1029/2002JC001463.

Hickey, B. (1995), Coastal submarine canyons, in *Topographic Effects in the Ocean*, edited by P. Müller and D. Henderson, pp. 95–110, Sch. of Ocean and Earth Sci. and Technol., Honolulu.

Hotchkiss, F., and C. Wunsch (1982), Internal waves in hudson canyon with possible geological implications, *Deep Sea Res.*, *29*(4A), 415–442.

Hsieh, W. (2009), *Machine Learning Methods in the Environmental Sciences*, Cambridge Univ. Press, Cambridge, U. K.

Huthnance, J. (1989), Internal tides and waves near the continental shelf edge, *Geophys. Astrophys. Fluid Dyn.*, *48*, 81–106.

Kunze, E., L. Rosenfeld, G. Carter, and M. Gregg (2002), Internal wave in Monterey Submarine Canyon, *J. Phys. Oceanogr.*, *32*, 1890–1913.

Lee, I., R. Lien, J. Liu, and W. Chuang (2009), Turbulent mixing and internal tides in Gaoping (Kaoping) Submarine Canyon, Taiwan, *J. Mar. Syst.*, *76*, 397–404.

McPhee-Shaw, E. (2006), Boundary-interior exchange: Reviewing the idea that internal-wave mixing enhances lateral dispersal near continental margins, *Deep Sea Res. Part II*, *53*, 42–59.

McPhee-Shaw, E., R. Sternberg, B. Mullenbach, and A. Ogston (2004), Observations of intermediate nepheloid layers on the northern California continental margin, *Cont. Shelf Res.*, *24*, 693–720.

Monteiro, P., G. Nelson, A. van der Plas, E. Mabille, G. W. Bailey, and E. Klingelhoeffer (2005), Internal tide-shelf topography interactions as a forcing factor governing the large-scale distribution and burial fluxes of particulate organic matter (POM) in the Benguela upwelling system, *Cont. Shelf Res.*, *25*, 1864–1876.

Munk, W. (1997), Once again: Once again—Tidal friction, *Prog. Oceanogr.*, *40*, 7–35.

Pawlowicz, R. (2002), Observations and linear analysis of sill-generated internal tides and estuarine flow in Haro Strait, *J. Geophys. Res.*, *107*(C6), 3056, doi:10.1029/2000JC000504.

Pawlowicz, R., B. Beardsley, and S. Lentz (2002), Harmonic analysis including error estimates in MATLAB using t_tide, *Comput. Geosci.*, *28*, 929–937.

Pérenne, N., D. Haidvogel, and D. Boyer (2001), Laboratory-numerical model comparisons of flow over a coastal canyon, *J. Atmos. Oceanic Technol.*, *18*, 235–255.

Petruncio, E., L. Rosenfeld, and J. Paduan (1998), Observations of the internal tide in Monterey Canyon, *J. Phys. Oceanogr.*, *28*, 1873–1903.

Petruncio, E., J. Paduan, and L. Rosenfeld (2002), Numerical simulations of the internal tide in a submarine canyon, *Ocean Modell.*, *4*, 221–248.

Pond, S., and G. Pickard (1983), *Introductory Dynamical Oceanography*, 2nd ed., Pergamon, Oxford, U. K.

Sandstrom, H., and J. Elliot (1984), Internal tides and solitons on the Scotian Shelf: A nutrient pump at work, *J. Geophys. Res.*, *89*, 6415–6426.

Sandstrom, H., and J. Elliot (2002), Tidal mixing and the Gully ecosystem, in *Advances in Understanding the Gully Ecosystem*, edited by D. Gordon Jr. and D. Fenton, pp. 49–56, Fish. and Oceans Can., Ottawa.

Shepard, F., N. Marshall, P. McLoughlin, and G. Sullivan (1979), *Currents in Submarine Canyons and Other Seavalleys*, *Stud. Geol. Ser.*, vol. 5, Am. Assoc. of Pet. Geol., Tulsa, Okla.

Strain, P., and P. Yeats (2005), Nutrients in the Gully, Scotian Shelf, Canada, *Atmos.-Ocean*, *43*, 145–161.

Thomsen, L., and T. van Weering (1998), Spatial and temporal variability of particulate matter in the benthic boundary layer at the N.W. European Continental Margin (Goban Spur), *Prog. Oceanogr.*, *42*, 61–76.

Torrence, C., and G. Compo (1998), A practical guide to wavelet analysis, *Bull. Am. Meteorol. Soc.*, *79*, 61–78.

Wang, Y., I. Lee, and J. Liu (2008), Observation of internal tidal currents in the Kaoping Canyon off southwestern Taiwan, *Estuarine Coastal Shelf Sci.*, *80*, 153–160.

Wunsch, C. (1969), Progressive internal waves on slopes, *J. Fluid Mech.*, *35*, 131–144.

Wunsch, C. (1975), Internal tides in the ocean, *Rev.f Geophys. Space Phys.*, *13*(1), 167–182.

Wunsch, C., and R. Ferrari (2004), Vertical mixing, energy and the general circulation of the oceans, *Ann. Rev. Fluid Mech.*, *36*, 281–314.

S. Allen, Department of Earth and Ocean Science, University of British Columbia, 6339 Stores Rd., Vancouver, BC V6T1Z4, Canada.

B. Greenan, Ocean Circulation Section, Ocean Sciences Division, Fisheries and Oceans Canada, Bedford Institute of Oceanography, PO Box 1006, 1 Challenger Dr., Dartmouth, NS B2Y 4A2, Canada.

N. Swart, School of Earth and Ocean Sciences, University of Victoria, 3800 Finnerty Rd., Victoria, BC V8P 5C2, Canada. (ncswart@uvic.ca)